

Multipolar young planetary nebulae modeled as a precessing and orbiting jet with time-dependent ejection velocity

Pablo F. Velázquez^{1*}, Alejandro C. Raga¹, Angels Riera^{2,3}, Wolfgang Steffen⁴,
Alejandro Esquivel¹, Jorge Cantó⁵, and Sinhué Haro-Corzo¹

¹*Instituto de Ciencias Nucleares, Universidad Nacional Autónoma de México, México D.F., México*

²*Departament de Física i Enginyeria Nuclear, EUETIB, Universitat Politècnica de Catalunya, Compte d'Urgell 187, 08036 Barcelona, Spain*

³*Departament d'Astronomia i Meteorologia, Universitat de Barcelona, Av. Diagonal 647, 08028 Barcelona, Spain*

⁴*Instituto de Astronomía, Universidad Nacional Autónoma de México, Ensenada, México*

⁵*Instituto de Astronomía, Universidad Nacional Autónoma de México, Apdo. Postal 70-242, CP: 04510, D.F., México*

Accepted to be published in MNRAS. Received —; in original form —

ABSTRACT

We have carried out 3D hydrodynamic simulations of precessing, variable ejection velocity bipolar jets in order to model multipolar proto-planetary (or planetary) nebulae. For these nebulae, we assume a binary source, with an AGB primary star which ejects an isotropic wind, and a companion which ejects the bipolar jet system. We find that it is possible to relate the large scale morphological characteristics of these nebulae (lobe size, semi-aperture angle, number of observed lobes) to some of the parameters of the binary system, such as the ratio between the orbital and precession periods, the ratio between the masses of the binary components, and the major axis of the elliptical orbit. Our results show that synthetic nebulae with well defined lobe morphologies (resembling many of the observed multipolar PNe) are obtained from our models.

Key words: hydrodynamics – methods: numerical – ISM: planetary nebulae: general – ISM: jets and outflows

1 INTRODUCTION

Young PPNe and PNe often exhibit a very rich morphology (e.g., elliptical, bipolar, or multipolar), with strong deviations from spherical symmetry. Bipolar or multipolar PPNe show one or more pairs of elongated structures or lobes, which seem to be ejected by the central star. Such structures can have a global mirror- or point-symmetric morphology.

The existence of a binary system inside these objects has been invoked as a mechanism to generate multi-lobe morphologies in young PPNe and PNe, as originally suggested by Bond et al. (1978) (also Livio et al. 1979; Soker & Livio 1994). This suggestion is supported by the increasing number of binary systems found inside bipolar/multipolar PNe. Bond (2000) carried out a survey showing that at least 10 % of PNe have binary systems with short orbital periods (<16 days). This fraction is low in comparison with the large fraction of bipolar or multipolar PNe. However, they could be the tip of the iceberg of a substantial population with longer orbital periods, still undetected because the observa-

tional technique employed in this survey cannot detect large orbital periods (Bond 2000). Miszalski et al. (2009) carried out the most up to date and robust measurement of the binary fraction, estimating a value of $17 \pm 5\%$.

Miranda (2002) (also Miranda et al. 2001a,b) presented an indirect observational method for detection of binary systems inside of PPNe and PNe. Their method is based to find differences in the systemic velocity of a bipolar outflows and the main shell of these objects, which would reveal the orbital motion. This method was employed for the cases of PN Hu 2-1 (Miranda et al. 2001b) and PN IC 4846 (Miranda et al. 2001a) obtaining orbital radius ≤ 30 AU and orbital periods ≤ 100 yr.

The model for building bipolar PNe and PPNe is based on considering a bipolar jet outflow (or collimated fast winds -CFW-) ejected by one of the components of a binary system (e. g. Morris 1987; Soker & Rappaport 2000). Sahai & Trauger (1998) showed that such jets can actually play a primary role in forming bipolar PPNe (see also Balick & Frank 2002). One of the stellar components of the binary system accretes material from its companion, forming a disk. Then, a pair of bipolar jets or CFWs are ejected along the axis

* E-mail: pablo@nucleares.unam.mx (PFV)

of the accretion disk (Frank & Blackman 2004; Frank et al. 2007).

The use of jets (continuous, time-dependent, and/or precessing) have been quite successful in explaining the global shape of several bipolar PNe and PPNe such as PPN CRL 618 (Lee & Sahai 2003), PPN Hen 3-1475 (Velázquez et al. 2004; Riera et al. 2004), PN K 3-35 (Velázquez et al. 2007), PN IC 4634 (Guerrero et al. 2008), and the Red Rectangle (RR) PPN (Velázquez et al. 2011). Akashi & Soker (2008) studied the shaping of PNe by light jets, using 2D axisymmetrical hydrodynamical simulationa. Raga et al. (2009) carried out an analytical and numerical study to explain how both mirror and point-symmetric morphologies can be obtained from a precessing jet from a binary system. Haro-Corzo et al. (2009) analyzed the influence of the orbital motion on the optical emission of these objects, by means of 3D HD simulations. They found that these models could display mirror or point-symmetric distributions, depending on the orientation of the flow with respect to the observer. Finally, Miszalski et al. (2011) and Corradi et al. (2011) have found direct observational support of the association of multi-lobe structures and close binary sources for the cases of PNe G068.1+11.0 and IPHASX J194359.5+170901, respectively.

Sahai (2000) identify multipolar young PNe and PPNe as “starfish” PNe. Such nebulae have been previously modeled considering the interaction of an isotropic, fast stellar wind with a warped accretion disk (Rijkhorst et al. 2005). With this scenario, Rijkhorst et al. (2005) studied the initial phases of the formation of this kind of PNe. As a result of such an interaction, multipolar morphologies are produced in the synthetic H α emission maps generated from their numerical simulations, at scales of ~ 10 times the accretion disk radius r_d ($\sim 10^{15}$ cm). Recently, García-Segura (2010) has suggested that multi-polar structures in PPN might be seeded or formed from thin-shell instabilities of the photo-dissociation front before the star becomes hot enough to ionize the gas and form a planetary nebula.

In the present work, we study another possibility, following the results obtained in Raga et al. (2009); Haro-Corzo et al. (2009); Velázquez et al. (2011). The main goal of this work is to explore if the formation of multipolar PPNe and PNe at large scales ($\sim 10^{17}$ cm) can be due to a precessing and orbiting jet, with a time-dependent ejection velocity. The input parameters have been chosen taking into account the observed characteristics of these objects, such as typical size, outflow velocities, and number of observed lobes. With this input, 3D hydrodynamical simulations were performed with the adaptive grid YGUAZÚ-A code. From the numerical results, both synthetic and position-velocity (PV) diagrams were generated.

This work is organized as follows: section 2 presents the adopted scenario and the theoretical background. Section 3 describes the characteristics of the YGUAZÚ-A code and the initial conditions of the numerical simulations. Section 4 shows presents the main results, and our conclusions are given in section 5.

2 MODELING MULTIPOLAR PPNE BY A PRECESSING AND ORBITING JET

2.1 Basic ideas

We explore if the multipolar morphology of this kind of PPNe can be reproduced by the interaction of a bipolar outflow (from one of the components of the central binary system) with the surrounding environment giving by the AGB wind. We will consider that the outflow source follows an elliptical orbit (around of the center of mass), with an eccentricity ϵ .

We define a system such that the orbit lies on the xy -plane, with the major axis aligned with the y axis (see the left panel of Figure 1). The companion star, with mass m_1 , accretes material from the primary star, of mass m_2 , and forms an accretion disk. A collimated outflow or jet is launched perpendicular to this accretion disk, with velocity v_j . The jet axis (lying along the orbital axis of the central region of the accretion disk) has a precession motion retrograde with respect to the orbital motion. The direction of the ejection is modified by the precession and the orbital motion.

The trajectory of the material along a jet is affected by the additional velocity component due to the presence of an orbital motion or a precession. If we only consider an orbital motion of the source, the jet/counter-jet system would describe a spiral path with mirror symmetry with respect to the plane of the orbit. If we only consider a precession, the jet/counter-jet system would trace a spiral path with point symmetry. In the presence of both an orbital motion and a precession, the resulting jet path would be a superposition of these two types of spiral (see Raga et al. 2009). For the case of a ballistic jet the step of the precession spiral (projected onto a plane which includes the precession axis) has a size:

$$D_p = v_j \cos \alpha \tau_p, \quad (1)$$

where v_j is the jet velocity, α is the semi-aperture angle of the precession cone and τ_p the precession period. In a similar manner, the effects of the orbital motion will produce a spiral with a step:

$$D_o = v_j \tau_o, \quad (2)$$

where τ_o is the orbital period. This spiral has a semi-aperture angle $\beta = \arctan(v_o/v_j)$, where v_o is the orbital speed. Since we usually have $\tau_p/\tau_o > 1$ (Terquem et al. 1999), we expect the effects of the orbital motion to be noticeable at distances close to the source ($\sim D_o$), while in contrast, the influence of the precession motion will become apparent at greater distances ($\sim D_p$).

Let us denote by D_l the size of the observed lobes in PPNe and young PNe (typically of the order of few 10^{17} cm). As a first approach we relate D_l to the precession scale (D_p) by $D_l = p D_p$, and obtain a characteristic time :

$$\tau = \frac{D_l}{v_j \cos \alpha} = p \tau_p. \quad (3)$$

The factor p represents the number of steps of the precession spiral which are present within one of the two sides of the outflow. This is considered as a free parameter.

The $q = \tau_p/\tau_o$ ratio has been found to depend on

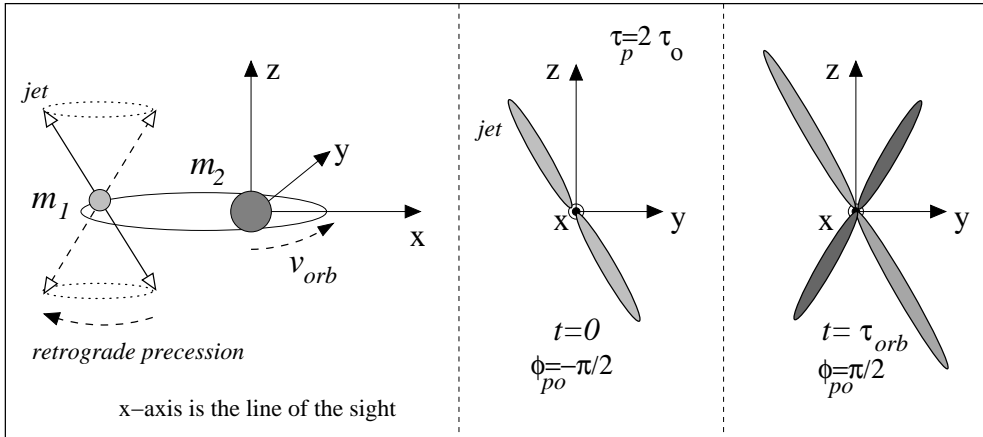


Figure 1. Schematic diagram of the initial conditions to generate a four-lobed PN, considering the case with $q = \tau_p/\tau_o = 2$. The precession is retrograde with respect to the orbital motion.

m_2/m_1 , the ratio of the stellar masses in the binary system (see Terquem et al. 1999, and Raga et al. 2009).

Using Eq.(3), τ_o can be written as:

$$\tau_o = \frac{D_l}{p q v_j \cos \alpha}. \quad (4)$$

The q parameter can be estimated from observations, as discussed in section 2.2.

With the orbital period (given by Eq. 4), the m_2/m_1 ratio, and a value for either m_1 or m_2 , we can calculate the semi-major axis a and the maximum orbital speed, which are given by:

$$a = [\tau_o^2 (m_1 + m_2)]^{1/3} \text{A.U.}, \quad \text{and} \quad (5)$$

$$v_{omax} = \frac{2\pi a}{\tau_o} \sqrt{\frac{1+\epsilon}{1-\epsilon}}, \quad (6)$$

where ϵ is the eccentricity of the orbit, m_1 and m_2 are given in units of M_\odot , and τ_o in yr.

2.2 How to generate a multipolar structure

A precessing and orbiting jet is not able by itself to produce a well-defined multipolar-lobe morphology. In order to achieve this, a variability in the jet ejection (either in velocity or in density) has to be introduced. In our work we choose a jet with a time-dependent velocity. For this ejection velocity variability, we consider a period equal to τ_o , assuming that the successive “ejection events” occur when the outflow source passes through the periastron of its elliptical orbit. This choice is supported by observational results of the central binary system of the RR PPN (Witt et al. 2009).

This ejection variability is the mechanism to generate multiple lobes. Thus the number of generated lobes is $2q$ (see equation 4). However, due to projection effects some of these lobes can overlap each other, so that the number of observed lobes will be $\leq 2q$.

For example, let us consider the production of a four-lobed synthetic nebula. We first set $q = 2$. At $t = 0$ both the jet and counter-jet are launched with maximum velocity $v_{jmax} = v_j + \Delta v$ (being v_j the mean jet velocity and Δv the amplitude of the jet velocity variability), when the jet

source passes through its periastron. The projection of the jet on the xy -plane (i. e., the orbital plane), forms an angle $\phi_p = -\pi/2$ with respect to the x -axis (as shown in the central panel of Figure 1). After a time τ_o , the jet velocity again achieves its maximum value and its direction in the orbital plane has changed by π radians due to the precession (see the right panel of Figure 1). This system will evolve to produce a four-lobed synthetic nebula, if the observer is located along the x -direction. On the other hand, if the line of sight of the observer is along the y -axis, the predicted morphology of the nebula will have a bipolar morphology.

Similarly, one can obtain a nebular morphology with four apparent lobes and $q = 4$ (eight real lobes). For instance, the jet is initially launched with v_{jmax} at an angle $\phi_p = \pi/4$ with respect to the x -axis. The three subsequent “launchings” with v_{jmax} will occur when the projected jet direction onto the orbital plane forms angles of $3\pi/4$, $5\pi/4$, $7\pi/4$ with respect to the x -axis. Therefore, the apparent morphology of a nebula with four lobes is due to the overlapping of pairs flows that move toward and away from the observer (located along the x - or y - axes).

3 CODE DESCRIPTION AND INITIAL NUMERICAL SIMULATION SETUP

The 3D numerical simulations were performed with the YGUAZÚ-A hydrodynamical code (Raga et al. 2000), which integrates the gasdynamical equations with a second order accurate scheme (in time and space) using the “flux-vector splitting” method of van Leer (1982) on a binary adaptive grid. A rate equation for neutral hydrogen is integrated together with the gas-dynamic equations to include the radiative losses through a parametrized cooling function that depends on the density, temperature and hydrogen ionization fraction (Raga & Reipurth 2004). The time-dependent cooling function is plotted in Figure 1 of Velázquez et al. (2011), for a gas parcel that cools at a constant (atom+ion) number density $n = 1 \text{ cm}^{-3}$.

We have employed a computational domain of $(1.25, 1.25, 2.5) \times 10^{17} \text{ cm}$ along the x -, y -, and z - axis, respectively, which are typical sizes of multipolar nebulae. An adaptive Cartesian grid with five refinement levels was used,

Table 1. Parameters employed in the models

model	τ (s)	$q = \tau_p/\tau_o$	τ_o (s)	α ($^\circ$)	m_2/m_1	Δv (km s $^{-1}$)	a(A.U.)	ϕ_{po}	$v_{o,max}$ (km s $^{-1}$)
M1	4×10^9	2	10^9	10.	10.0	75.0	14.9	$-\pi/2$	24.3
M2	4×10^9	4	5×10^8	15.	3.0	75.0	6.7	$\pi/4$	21.9
M3	4.4×10^9	3	7.4×10^8	30.	5.0	75.0	10.0	0.	22.1
M4	4.4×10^9	4	5.5×10^8	30.	3.0	75.0	7.1	0.	21.0
M5	4.4×10^9	6	3.7×10^8	30.	1.5	75.0	4.7	$\pi/3$	20.7
M6	4×10^9	4	5×10^8	15.	3.0	0.0	6.7	$\pi/4$	21.9
M7	4×10^9	4	5×10^8	15.	3.0	37.5	6.7	$\pi/4$	21.9

achieving a resolution of $\sim 4.9 \times 10^{14}$ cm at the finest level, corresponding to $(256 \times 256 \times 512)$ pixels in an uniform grid.

We assume that the jet is launched from the companion star. This jet propagates into an environment given by the dense and slow wind from the AGB primary star. At the initial time (and filling the whole computational domain), we impose an isotropic, constant velocity AGB wind with a density distribution given by :

$$\rho_w = \frac{\dot{M}_w}{4\pi r^2 v_w}, \quad (7)$$

where r is the distance from the primary star, \dot{M}_w is the mass loss rate of the AGB wind, and v_w is the terminal wind velocity. We have assumed $\dot{M}_w = 2 \times 10^{-6} M_\odot \text{ yr}^{-1}$, $v_w = 15 \text{ km s}^{-1}$, and a constant temperature $T_w = 100 \text{ K}$. This initial constant temperature acquires a decreasing profile with distance r , as time-integration proceeds.

The jet/counter-jet system is injected at the center of the computational domain inside a cylindrical volume with radius r_j and length l_j , both equal to 3×10^{15} cm (equivalent to 6 pixels in the finest grid). The jet axis precesses describing a cone with a semi-aperture angle α and period τ_p . Seven models were computed considering different values for these parameters (see Table 1). We have chosen $\alpha = 10^\circ$ for model M1, $\alpha = 15^\circ$ for models M2, M6, and M7, and $\alpha = 30^\circ$ for models M3, M4, and M5. At $t = 0$, the jet direction projected on the orbital plane forms an angle ϕ_{po} with respect to the x -axis (see Table 1).

The mean jet velocity v_j and initial number density n_j were set to 250 km s^{-1} and $5 \times 10^4 \text{ cm}^{-3}$, respectively. With these values, the average mass injection rate of the jet is $\dot{M}_j = 2.4 \times 10^{-6} M_\odot \text{ yr}^{-1}$. In $\sim 200 \text{ yr}$ (the total integration time of our simulations) both the jet and counter-jet inject into the surrounding medium a total mass of $4.8 \times 10^{-4} M_\odot$.

Models M1-M5 have a sinusoidal velocity variability with an amplitude Δv of 75 km s^{-1} , while model M7 has $\Delta v = 37.5 \text{ km s}^{-1}$. We have assumed that the velocity variability period is equal to the orbital period τ_o . If the orbit is elliptical, we expect that the accretion, and also the jet launching, would be more efficient when the stars pass through the periastron. This behaviour was found for the case of the binary system inside the RR PPN (Witt et al. 2009). To contrast with the results with a variable velocity, we included model M6 in which the jet velocity is constant. In Cartesian coordinates we can write the three components of the jet velocity as:

$$v_x = v_j \sin \alpha \cos(\omega_p t) + v_{ox} \quad (8)$$

$$v_y = -v_j \sin \alpha \sin(\omega_p t) + v_{oy} \quad (9)$$

$$v_z = v_j \cos \alpha \quad (10)$$

where ω_p is precession angular frequency, and v_{ox} and v_{oy} are the x - and y - components of the orbital speed. We have set the eccentricity to 0.5 in all the models.

For simplicity in all models we have assumed $p = 2$. The parameter q was set 2 (model M1), 3 (model M3), 4 (models M4, M6, and M7), and 6 (model M5).

We now estimate the characteristic time of dynamical evolution τ . Considering Eq.(3), with $D_l \simeq 1.25 \times 10^{17} \text{ cm}$, a maximum velocity of 325 km s^{-1} , and the values for α listed in Table 1, we obtain $\tau = 4 \times 10^9 \text{ s}$ ($\simeq 127 \text{ yr}$) for models M1, M2, M6 and M7, and for models M3, M4 and M5 we obtain $\tau = 4.4 \times 10^9 \text{ s}$ ($\simeq 140 \text{ yr}$).

Knowing the value of $q = \tau_p/\tau_o$, we can estimate the m_2/m_1 ratio (Terquem et al. 1999; Raga et al. 2009), and setting $m_1 = 0.3 M_\odot$ we can calculate the major semi-axis and the maximum orbital speed of the elliptical orbit (see Table 1, Eqs (5) and (6)) for all models.

4 RESULTS

4.1 Forming four- and six-lobed “synthetic nebulae”

We have carried out seven runs with the parameters listed in Table 1. From the numerical results, we have calculated synthetic H α emission maps. As discussed in subsection 2.2, an apparent four-lobed synthetic nebula can be obtained if we set $q = 2$ (model M1) or $q = 4$ (model M2). This morphology is clearly observed in Figure 2, in the yz -projection for both models, and in the xz -projection of model M2. The xz -projection of run M1 shows several knots distributed along the vertical axis. Point-symmetric morphologies are obtained for the yz - and xz -projections of models M1 and M2, respectively, showing two opposite lobes which are more developed than the other two lobes. The global four-lobed morphology of the yz -projection of M2 has an almost mirror symmetric shape, although the knots inside of the lobes exhibit a point-symmetric distribution¹

To get an “apparent” six-lobed morphology, we have carried out the M3, M4 and M5 runs, with $q = 3, 4$ and 6 , respectively. The resulting synthetic H α emission maps

¹ Three-dimensional animations of the nebula structure and PV diagrams corresponding to models M1 and M2 were generated using SHAPE (Steffen et al. 2011), which can be viewed at <http://www.nucleares.unam.mx/astroplasma/index.php/gallery/science-gallery>.

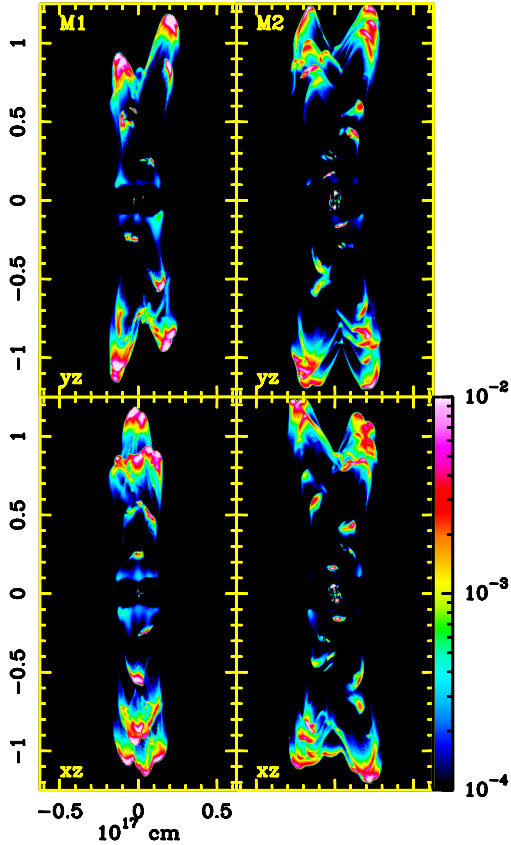


Figure 2. Synthetic H α emission maps obtained from models M1 (left panels) and M2 (right panels). Upper panels display the yz projection for both models, while bottom panels show the xz projection. The angle between the projection maps and the plane of the sky was set to 0 for all models. The vertical color bar gives the H α flux in units of $\text{erg s}^{-1}\text{cm}^{-2}\text{sr}^{-1}$. Vertical and horizontal axes are in units of 10^{17} cm.

are shown in Figure 3 and a pattern of six lobes is clearly seen in the yz projection of the three models, and in the xz projection of model M4. The central lobes of all yz -maps show a deviation to the right ($+\hat{y}$ direction). This is produced by the orbital motion because the lobes are launched, at $t = 0$, along the line of sight (the x -direction) with zero velocity along the y -axis due to the precession motion. In this direction, the orbital speed achieves its maximum value, producing the same deviation for both the top and bottom central lobes. The xz map of model M3 has a four-lobe pattern, two of which (the top left and the bottom right lobe) appear wider than the remaining two lobes. These observed lobes are the result of the overlapping of two or more outflow episodes moving along the line of sight. Instead, the xz projection of the H α intensity of model M5 exhibits a structure with 8 lobes.

Figure 4 shows a “top view” (the z -axis from an angle of 90° with respect to the plane of the sky) of the H α emission for all models, which show structures with several ripples.

4.2 PV diagrams

Models M1 and M2 have a structure of four similar lobes in their yz projection. However, it is possible to distinguish

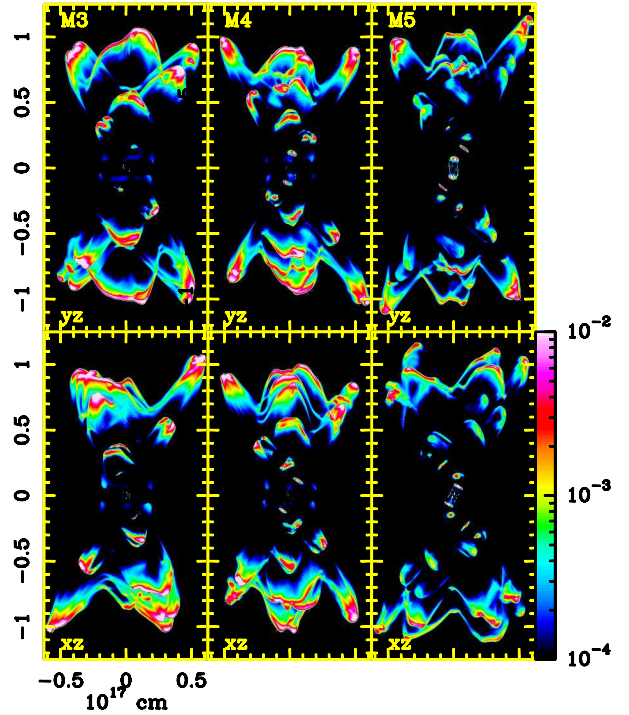


Figure 3. Same as Fig. 2 but for models M3 (left panels), M4 (middle panels), and M5 (right panels).

them by means of an analysis of their PV diagrams. These PV diagrams were generated considering a broad slit, which covers all the horizontal axis of the synthetic maps. Also, it was considered that the angle between the plane of the sky and the z -axis is zero.

Figure 5 shows a comparison between the yz images and corresponding PV diagrams of M1 and M2. The four-lobed morphology obtained from model M1 has a pattern of several aligned knots centred at $v_r = 0 \text{ km s}^{-1}$, with maximum radial velocities $\sim 50 \text{ km s}^{-1}$. Instead, the mirror symmetric morphology displayed in the yz map of model M2 becomes a “point-symmetric” morphology in its corresponding PV diagram, with maximum radial velocities $\sim 80 \text{ km s}^{-1}$. Such a “point-symmetric” distribution in PV diagrams has been observed in the PN IC 4634 (Guerrero et al. 2008).

Also, the PV diagram of model M2 has large radial velocities at large distances from the source, which is observed in the “knots” located at the bottom right region of Fig. 5. Fig. 6 is an enlargement of the rectangular region shown in Fig. 5, revealing the existence of “ramps” of increasing radial velocity vs. position with respect to the source. Such radial velocity “ramps” are observed in some young PPN, such as PPN CRL 618 (Riera et al. 2009).

Figure 7 shows the yz H α maps of models M3, M4, and M5, and the corresponding PV diagrams. The PV diagrams reveal radial velocities of $\sim 180 \text{ km s}^{-1}$, and show a general “point-symmetric” distribution of the velocity structures.

Since the general velocity pattern is important for the reconstruction of the 3D structure based on Doppler-velocity measurements, note that the overall velocity pattern in model M2 is non-homologous. The knots near the center move faster or at the same speed as the outer knots that interact directly with the ambient medium. This is an inherent

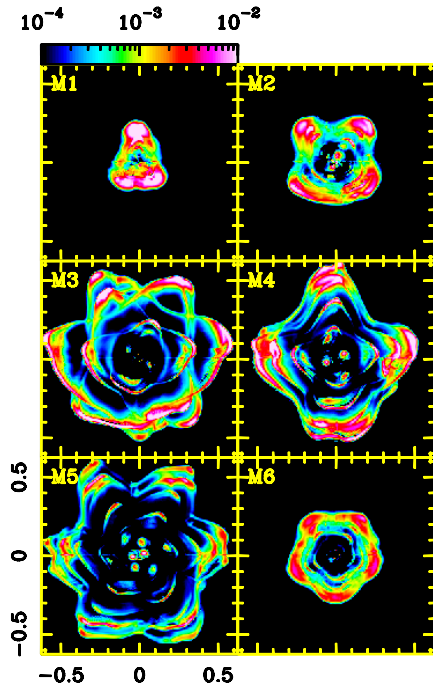


Figure 4. Comparison of the synthetic emission $H\alpha$ maps obtained from models M1-M6, for the case where the z -axis is tilted 90° with respect to the plane of the sky

feature of the model and distinctive from an explosive event. This non-homologous velocity field is also seen in models M3 to M5 (see Fig. 7).

4.3 Multipolar morphology vs. jet velocity variability

Figures 8 and 9 show the yz -projection of column density and synthetic $H\alpha$ maps for models M6, M7, and M2. Models M6 and M7 were carried out to explore the development of lobe-type structures as a function of the velocity variation.

A helical path is clearly seen in both the column density and $H\alpha$ emission maps obtained from model M6. This “path” is due to the jet precession motion, as was shown in Velázquez et al. (2011) for the case of the RR PPN. In model M6, the morphology of the resulting nebula obtained has two “heads” with a knotty structure in the synthetic $H\alpha$ maps, with no clear evidence of lobe formation.

The maps obtained from models M7 and M2 resemble each other, indicating that an ejection velocity variability is necessary to generate lobes. A well defined four-lobed structure is obtained by increasing the amplitude of the jet velocity variability (see the right panels of Figures 8 and 9).

5 DISCUSSION & CONCLUSIONS

In this work, we present a possible mechanism for explaining the formation of multipolar PPNs and PNe, based on the existence of a binary source which ejects a wind (from the primary star) and a bipolar, precessing jet (from the orbiting companion). This is a continuation of the work of Raga et al. (2009); Haro-Corzo et al. (2009); Velázquez et al. (2011).

We find that the number of observed lobes is related

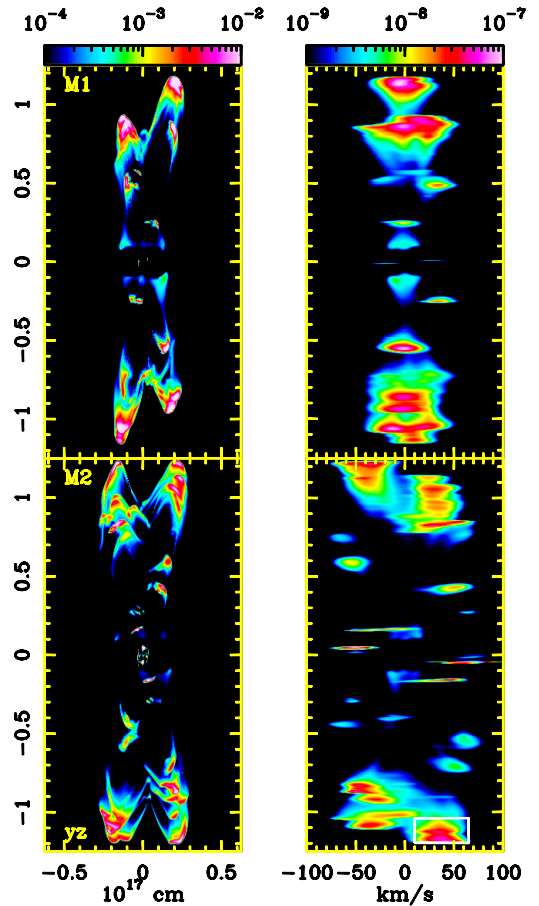


Figure 5. Comparison of synthetic emission maps (left panels) and PV diagrams (right panels) corresponding to models M1 and M2 (upper and bottom panels, respectively). All these maps consider the yz projection.

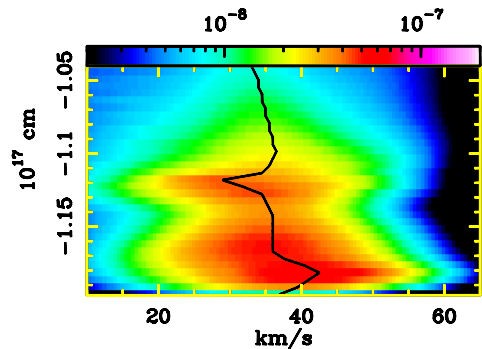


Figure 6. Enlargement of the rectangular region shown in Figure 5. The black line indicates positions of the maximum emission. We show that the radial velocity has a tendency to increase as a growing distance from the source.

to the parameter q , the ratio between the precession and orbital periods. Knowing q , we can obtain the mass ratio between the stellar components of the binary system. Then, taking into account the lobe size (which can be inferred from observations), and giving a value for the mass of one of the stellar components and for the jet velocity, we can estimate the orbital period and the orbital radius.

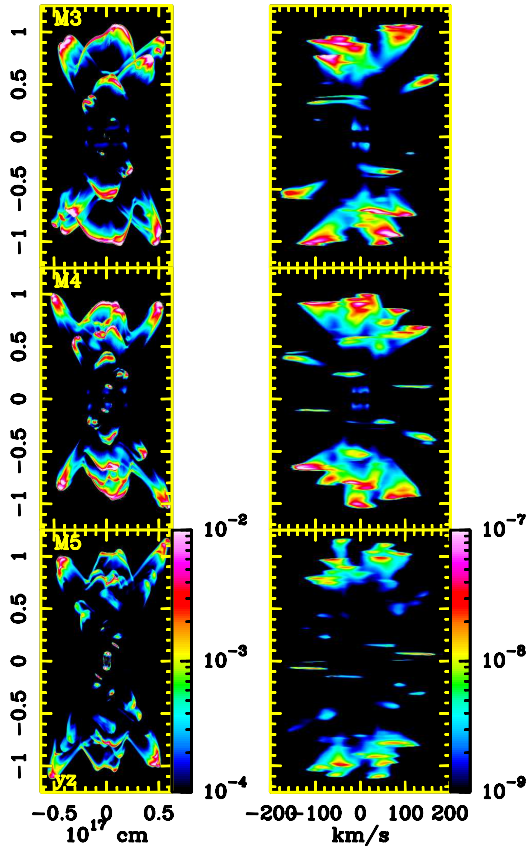


Figure 7. Same as Fig. 5 but for models M3 and M4 (upper and bottom panels, respectively).

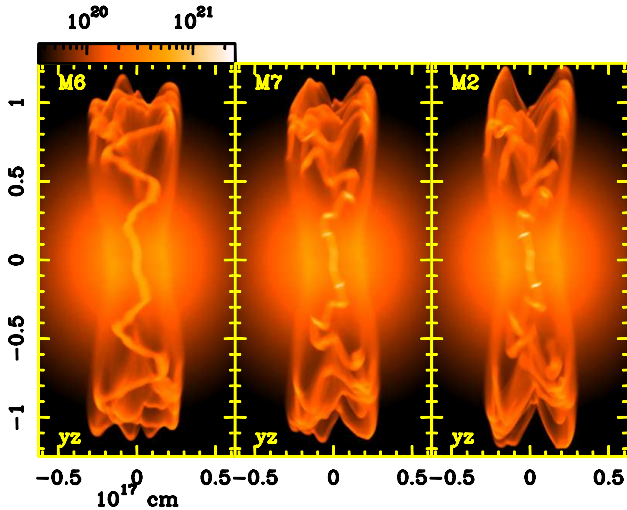


Figure 8. Comparison of column density maps generated from models M6, M7, and M2 (left, middle, and right panels, respectively). A helical path due to the jet precession motion is clearly seen in the left panel, which corresponds to the continuous precessing jet case

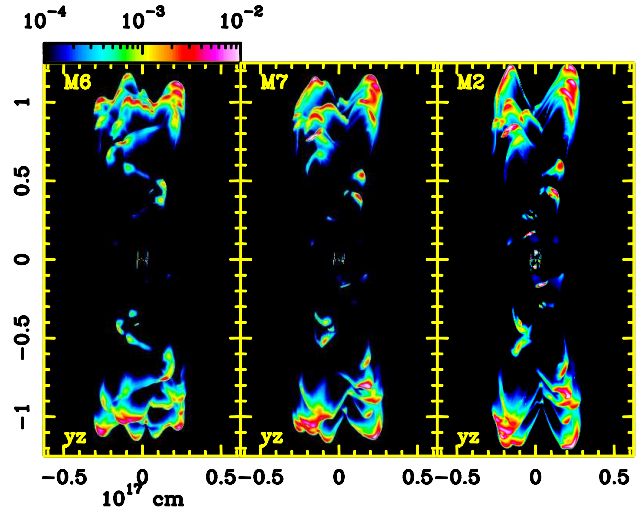


Figure 9. Synthetic H α emission maps obtained from models M6, M7, and M2 (left, middle, and right panels, respectively).

Several numerical simulations of a precessing and orbiting jet were carried out, in order to obtain synthetic multipolar nebulae. In particular, we explore how to obtain synthetic objects which exhibit two, four and six lobes. Well defined lobes are produced if we include a variability in the ejection velocity. We have assumed that the ejection velocity variability period is equal to the orbital period, which seems to be the case for the binary system inside RR PPN (Witt et al. 2009).

Different forms of the ejection variability are in principle possible. For example, one could assume that the ejection has a strong density variability, and an almost constant velocity. Another possibility that has been considered is that both the ejection density and velocity vary with time so as to keep a constant mass loss rate (see, e.g., Cantó et al. 2000). Such alternative forms for the outflow variability are not explored in our present work.

The resulting orbital periods (of several years) are larger than the periods reported in surveys of post-common-envelope binary systems inside PNe (Miszalski et al. 2009). However, the observational techniques used in these surveys are not (yet) able to detect such longer orbital periods.

The synthetic maps predicted from the numerical simulations show morphologies that can be qualitatively compared with images of multipolar nebulae. Furthermore, the PV diagrams are a useful tool to distinguish different cases, and can also be compared in a qualitative way with observations.

The exploration of model parameters discussed in the present paper will later have to be extended to parameters tuned to model specific multipolar nebulae. Such more detailed modeling will probably indicate the presence of more complex phenomena, but might corroborate the relevance of the general mechanisms discussed above.

ACKNOWLEDGMENTS

The authors thank the useful comments of the referee, which help us to improve the previous version of this manuscript. The authors thank Brent Miszalski for his very useful

comments and suggestions. We also thank Enrique Palacios for maintaining the linux servers where the simulations were performed. PFV, ACR, AE, and JC acknowledge support from the CONACyT grants 61547,101356, and 101975, and UNAM DGAPA grant PAPIIT IN119709. WS acknowledges support from UNAM DGAPA grant PAPIIT IN100410. The work of ARi was supported by the MICINN grant AYA2008-06189-C03 and AYA2008-04211-C02-01 (co-funded with FEDER funds).

REFERENCES

- Akashi, M., & Soker, N. 2008, *MNRAS*, 391, 1063
- Balick, B., & Frank, A. 2002, *ARA&A*, 40, 439
- Bond, H. E., Liller, W., & Mannery, E. J. 1978, *ApJ*, 223, 252
- Bond, H. E. 2000, *Asymmetrical Planetary Nebulae II: From Origins to Microstructures*, 199, 115
- Cantó, J., Raga, A. C., & D’Alessio, P. 2000, *MNRAS*, 313, 656
- Corradi, R. L. M., et al. 2011, *MNRAS*, 410, 1349
- Frank, A., & Blackman, E. G. 2004, *ApJ*, 614, 737
- Frank, A., De Marco, O., Blackman, E., & Balick, B. 2007, *arXiv:0712.2004*
- García-Segura, G. 2010, *A&A*, 520, L5
- Guerrero, M. A., et al. 2008, *ApJ*, 683, 272
- Haro-Corzo, S. A. R., Velázquez, P. F., Raga, A. C., Riera, A., & Kajdic, P. 2009, *ApJL*, 703, L18
- Lee, C.-F., & Sahai, R. 2003, *ApJ*, 586, 319
- Livio, M., Salzman, J., & Shaviv, G. 1979, *MNRAS*, 188, 1
- Masciadri, E., & Raga, A. C. 2002, *ApJ*, 568, 733
- Miranda, L. F. 2002, *Revista Mexicana de Astronomía y Astrofísica Conference Series*, 13, 145
- Miranda, L. F., Guerrero, M. A., & Torrelles, J. M. 2001, *MNRAS*, 322, 195
- Miranda, L. F., Torrelles, J. M., Guerrero, M. A., Vázquez, R., & Gómez, Y. 2001, *MNRAS*, 321, 487
- Miszalski, B., Acker, A., Moffat, A. F. J., Parker, Q. A., & Udalski, A. 2009, *A&A*, 496, 813
- Miszalski, B., Corradi, R. L. M., Boffin, H. M. J., Jones, D., Sabin, L., Santander-García, M., Rodríguez-Gil, P., & Rubio-Díez, M. M. 2011, *MNRAS*, 413, 1264
- Morris, M. 1987, *PASP*, 99, 1115
- Raga, A. C., Navarro-González, R., & Villagrán-Muniz, M. 2000, *RMxAA*, 36, 67
- Raga, A. C., Esquivel, A., Velázquez, P. F., Cantó, J., Haro-Corzo, S., Riera, A., & Rodríguez-González, A. 2009, *ApJL*, 707, L6
- Raga, A. C., & Reipurth, B. 2004, *RMxAA*, 40, 15
- Riera, A., Velázquez, P. F., & Raga, A. C. 2004, *Asymmetrical Planetary Nebulae III: Winds, Structure and the Thunderbird*, 313, 487
- Riera, A., Raga, A. C., Velázquez, P. F., Haro-Corzo, S., & Kajdic, P. 2009, *Protostellar Jets in Context*, 603
- Rijkhorst, E.-J., Mellema, G., & Icke, V. 2005, *A&A*, 444, 849
- Sahai, R., & Trauger, J. T. 1998, *AJ*, 116, 1357
- Sahai, R. 2000, *ApJL*, 537, L43
- Soker, N., & Livio, M. 1994, *ApJ*, 421, 219
- Soker, N., & Rappaport, S. 2000, *ApJ*, 538, 241
- Steffen, W., Koning, N., Wenger, S., Morisset, C., Magnor, M., 2011, *IEEE Transactions on Visualization and Computer Graphics*, 17, 454 .
- Terquem, C., Eisloffel, J., Papaloizou, J. C. B., & Nelson, R. P. 1999, *ApJL*, 512, L131
- van Leer, B. 1982, in *Lecture Notes in Physics*, Vol. 170, *Numerical Methods in Fluid Dynamics*, ed. E. Krause (Berlin:Springer)
- Velázquez, P. F., Riera, A., & Raga, A. C. 2004, *A&A*, 419, 991
- Velázquez, P. F., Gómez, Y., Esquivel, A., & Raga, A. C. 2007, *MNRAS*, 382, 1965
- Velázquez, P. F., Steffen, W., Raga, A. C., Haro-Corzo, S., Esquivel, A., Cantó, J., & Riera, A. 2011, *ApJ*, 734, 57
- Witt, A. N., Vijh, U. P., Hobbs, L. M., Aufdenberg, J. P., Thorburn, J. A., & York, D. G. 2009, *ApJ*, 693, 1946